Direct Monitoring of Coronary Artery Motion With Cardiac Fat Navigator Echoes

Thanh D. Nguyen, Anthony Nuval, Suresh Mulukutla, and Yi Wang*

Navigator echoes (NAVs) provide an effective means of monitoring physiological motion in magnetic resonance imaging (MRI). Motion artifacts can be suppressed by adjusting the data acquisition accordingly. The standard pencil-beam NAV has been used to detect diaphragm motion; however, it does not monitor cardiac motion effectively. Here we report a navigator approach that directly measures coronary artery motion by exciting the surrounding epicardial fat and sampling the signal with a *k*-space trajectory sensitized to various motion parameters. The present preliminary human study demonstrates that superior–inferior (SI) respiratory motion of the coronary arteries detected by the cardiac fat NAV highly correlates with SI diaphragmatic motion detected by the pencil-beam NAV. In addition, the cardiac fat navigator gating is slightly more effective than the diaphragmatic navigator gating in suppressing motion artifacts in free-breathing 3D coronary MR angiography (MRA). Magn Reson Med 50:235–241, 2003. © 2003 Wiley-Liss, Inc.

Key words: coronary magnetic resonance angiography; navigator echo; motion detection; motion artifacts; epicardial fat

Magnetic resonance imaging (MRI) has been identified as a very promising technology for noninvasive and comprehensive imaging of heart disease. One of the major technical challenges presented by MRI is the need to overcome image artifacts caused by physiologic motion, which is of particular concern in high-resolution coronary MR angiography (MRA), an important area of cardiac MRI. Current coronary MRA techniques employ electrocardiogram (ECG) gating for cardiac motion suppression, and a variety of methods for respiratory motion suppression, such as breath-holding (1,2) and the navigator approach (3). Breath-holding requires patient cooperation, limits available scan time, and does not eliminate motion (4). The navigator approach offers way to overcome these limitations by monitoring motion during scanning, and using motion information to guide data acquisition accordingly. When heart motion is accurately measured, the navigator approach can be very effective in suppressing motion artifacts in cardiac MRI.

The navigator echo (NAV) used in current coronary MRA often is the signal from a cranial-caudal cylinder of tissue oriented through the diaphragm and acquired using a 2D selective excitation pulse (pencil beam) (5). Because the respiratory movements of the diaphragm and the heart are correlated (6), the diaphragmatic NAV can be used to suppress respiratory motion artifacts in free-breathing coronary MRA (7–12). However, the reported sensitivity and specificity of the diaphragmatic navigator approach in detecting significant stenoses of the coronary arteries are a disappointing ~70% ± 20% (11,13–20), indicating significant variability in image quality. The need to identify and control factors that contribute to quality inconsistency is one of the most commanding topics in coronary MRA. One major factor is the diaphragmatic NAV itself, which does not directly monitor the motion of coronary arteries. The fact that hysteresis between the heart and the diaphragm may occur during the respiratory cycle (21) indicates that the diaphragmatic NAV is an inaccurate measure of coronary motion, which consequently limits its effectiveness for suppressing motion artifacts.

To improve navigator-gated coronary MRA, it is necessary to obtain direct, accurate measurements of coronary motion. The pencil-beam navigator can be applied to the left ventricle wall to directly monitor cardiac motion (22–23), but chamber blood motion complicates the navigator signal and makes it difficult to extract cardiac wall motion (22). In this work we propose a new navigator method, the cardiac fat NAV, for direct monitoring of the motion of epicardial fat that surrounds, and moves together with, the coronary arteries. Epicardial fat can be excited using spatial-spectral selective pulses and then sampled using multidimensional (e.g., orbital (24) or spherical (25)) *k*-space trajectories. The bulk or global motion of the epicardial fat can be extracted from the sampled navigator signal (26–28). Because >90% of coronary motion can be decomposed as global motion (translation, rotation, and dilation) (29), and coronary arteries and epicardial fat experience the same global motion, we hypothesize that the cardiac fat NAV provides a fast, direct measurement of bulk coronary artery motion without interfering with water-based coronary imaging.

In this work we describe our initial implementation of the cardiac fat NAV and report preliminary results from human imaging experiments, which validate the feasibility of this approach.

MATERIALS AND METHODS

Cardiac Fat NAV

The proximal coronary arteries are surrounded by the myocardium and epicardial fat, and a NAV can be acquired from either location to monitor coronary motion. Motion detection from the myocardial signal is complicated by the chamber blood, which has the same resonance frequency as the myocardium. Epicardial fat resonates at a different frequency from that of blood (by approximately 220 Hz at 1.5 T). It can be excited selectively using a spectral radiofrequency (RF) pulse, thereby allowing direct monitoring of coronary motion without interference
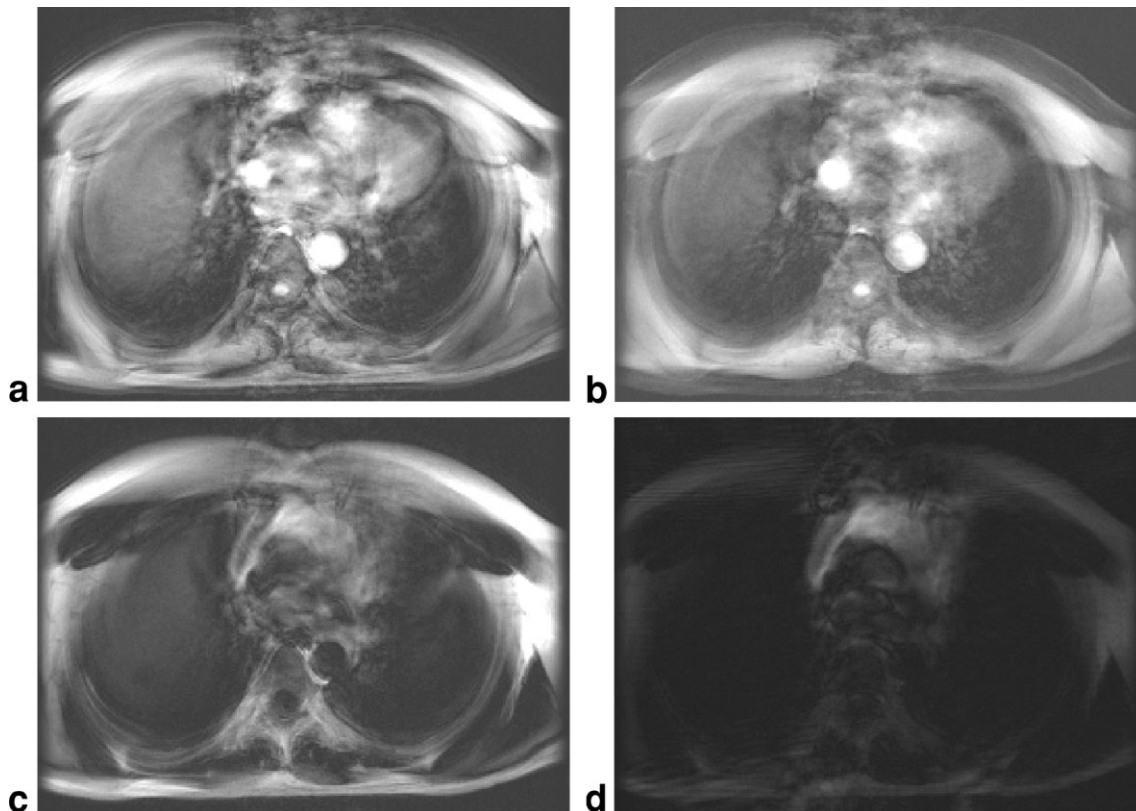
FIG. 1. Volume- and spectrum-selective excitation of epicardial fat: (**a**) water and fat image using SI-selective pulse, (**b**) water image using SI- and spectrum-selective pulse, (**c**) fat image using SI- and spectrum-selective pulse, and (**d**) epicardial fat image using SI-, RL-, AP- and spectrum-selective pulses (the RL and AP selection was achieved using 2D spatial saturation pulse). The prescribed volume is a 70-mm-thick slab containing the heart.

from the chamber blood. We refer to this navigator approach as the cardiac fat NAV.

The excitation of epicardial fat within the heart volume requires the use of volume- and spectrum-selective RF pulses. This can be accomplished by transmitting a 3D spatial saturation pulse to suppress the fat signals outside the six walls of the heart (i.e., the superior–inferior (SI), right–left (RL), and anterior–posterior (AP) walls) and then transmitting a 1D spectrum-selective pulse centered on the fat frequency. Another technique is to transmit a 2D spatial saturation pulse to suppress fat signals outside four walls of the heart, and then transmit a 2D spatial-spectral pulse that is spatially selective in the unsaturated direction of the heart and spectrally centered on the fat frequency. Other techniques are straightforward and follow this line of reasoning. In this preliminary implementation, a 2D spatial saturation pulse was used to suppress the fat signals from the RL and AP chest walls, followed by a 2D spatial-spectral pulse selective in the SI direction and centered on the fat frequency. The rationale behind this choice was that 2D spatial saturation pulses are readily available and the theory and practice of 2D spatial-spectral pulses are well understood (30–32). The volume- and spectrum-selective excitations in the cardiac fat NAV are illustrated in Fig. 1.

Immediately following the volume- and spectrum-selective excitations, the resultant epicardial fat signal is sam-

pled along a multidimensional k-space trajectory that sensitizes various global motion parameters (24,25). The present preliminary study employed a piecewise linear trajectory consisting of straight-line segments along k-space axes to detect the 3D bulk translation (Fig. 2a). This enabled a sensible comparison to be made with the existing pencil-beam navigator, which detects diaphragm displacement. Since this trajectory crosses the k-space origin three times, the resulting fat echo contains three peaks. The magnitudes of these peaks decrease following the T_2^* decay, and the phase changes reflect the displacements of the epicardial fat according to the Fourier shift theorem (33). Figure 2b shows an example of the k-space NAV profile acquired from a human volunteer, using a body coil.

Figure 3 summarizes the cardiac fat navigator pulses implemented in this preliminary study. The pulses consisted of spatial saturation pulses to suppress the chest wall signal (including fat), followed by 2D spatial-spectral pulses to excite the epicardial fat, and finally k-space sampling using readout and spoiler gradients. Hadamard RF pulses (34) were used in spatial saturation in order to combine the excitations of saturation bands (RL or AP bands) in the same direction for the purpose of shortening pulse duration when these parallel bands were of the same thickness. The 2D spatial-spectral RF pulse was a binomial 1-4-6-4-1 pulse (31,32) that used five RF subpulses of iden-
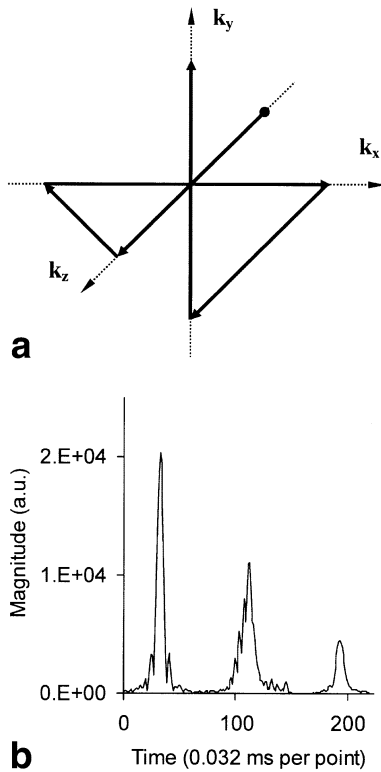
FIG. 2. **a:** Implemented *k*-space readout trajectory starting from negative k_z-axis and traversing through all three *k*-space axes. **b:** Corresponding MR signal magnitude profile sampled along the trajectory defined in **a**.

tical shape, as designed by the Shinnar-Le Roux algorithm (35), for a given pulse duration of 0.6 ms and bandwidth of 10 kHz.

Experiments

Experiments comparing the performance of the cardiac fat NAV with that of the diaphragmatic NAV were performed on healthy adults, using a 1.5 T whole-body MR scanner
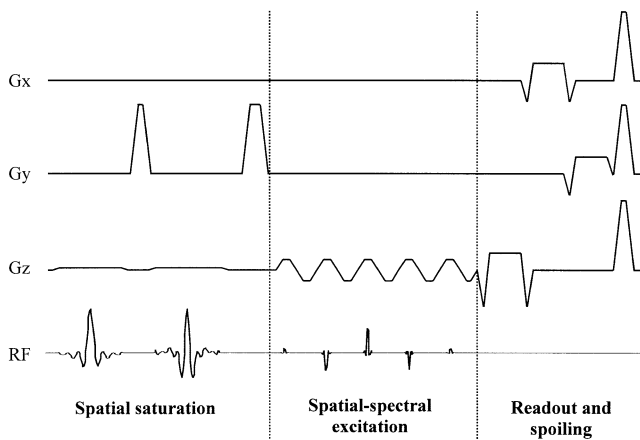

FIG. 3. Pulse sequence diagram of the cardiac fat NAV consisting of spatial saturation, spatial-spectral excitation, and *k*-space sampling (typical duration is 30–35 ms).
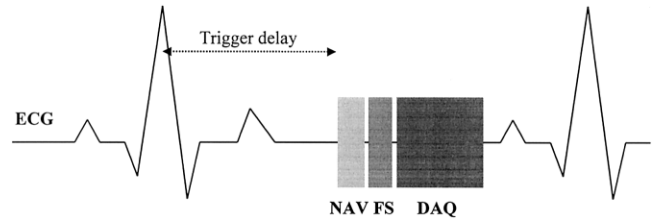

FIG. 4. Schematics for the ECG-triggered, navigator-gated, *k*-space-segmented, gradient-echo coronary MRA. After the ECG trigger delay, the NAV and fat saturation (FS) are executed, and data acquisition (DAQ) immediately follows.

(Signa CV/i; GE Medical Systems, Milwaukee, WI). This study was approved by our institutional review board, and written consent was obtained from all participants. The subjects were examined in a supine position with peripheral pulse gating during free breathing. A four-element, phased-array cardiac coil (two anterior and two posterior elements) was used for signal reception. The navigator *k*-space signal (Fig. 2b) was segmented into three echoes corresponding to the sampling along three *k*-space axes, and each echo was Fourier transformed to image space. Displacements were extracted from these image-space navigator signals using a least-squares motion extraction algorithm (26).

For the purposes of navigator positioning and coronary artery localization, three scout scans were obtained (36). The first scout scan acquired a series of sagittal images to determine the location of the heart (ungated 2D fast spoiled gradient-echo, TR = 6 ms, TE = 1.3 ms, flip angle = 20°, readout bandwidth (rbw) = ±31.25 kHz, field of view (FOV) = 400 mm, matrix = 256 × 160, and slice thickness = 10 mm with no slice gap). From these images, both diaphragmatic and cardiac fat navigator positions were determined. In addition, the second axial scout scan was prescribed to locate the septum (ungated 2D fast spoiled gradient-echo, TR = 6 ms, TE = 1.3 ms, flip angle = 20°, rbw = ±31.25 kHz, FOV = 320 mm, matrix = 256 × 160, slice thickness = 4 mm with 1-mm slice gap). For the third scout, single-oblique cine scans parallel to the septum and through the right atrioventricular (AV) sulcus at the right edge of the heart were prescribed on the axial images of the second scout (TR = 18 ms, TE = 3.2 ms, flip angle = 20°, rbw = ±31.25 kHz, FOV = 300 mm, matrix = 256 × 160, four slices, slice thickness = 4 mm with 1-mm slice gap, and 16 cardiac phases). From the oblique images of the AV sulcus, a double-oblique volume could then be prescribed to image the right coronary artery (RCA). The optimal delay time between the cardiac trigger and the mid-diastole, the period of minimal cardiac contraction (rest period), was also determined from these cine images. An additional axial scan was acquired to ensure proper positioning of the RL and AP saturation bands (2D ungated spoiled gradient-echo, TR = 50 ms, TE = 7.3 ms, rbw = ±31.25 kHz, FOV = 300 mm, matrix = 256 × 160, one slab, slab thickness = 50–80 mm, 1-4-6-4-1 type I spatial-spectral RF pulse centered on fat frequency, flip angle = 30°, RL and AP spatial saturation—same slab thickness, RF excitation pulse, and the same saturation bands as used for the cardiac fat NAV).
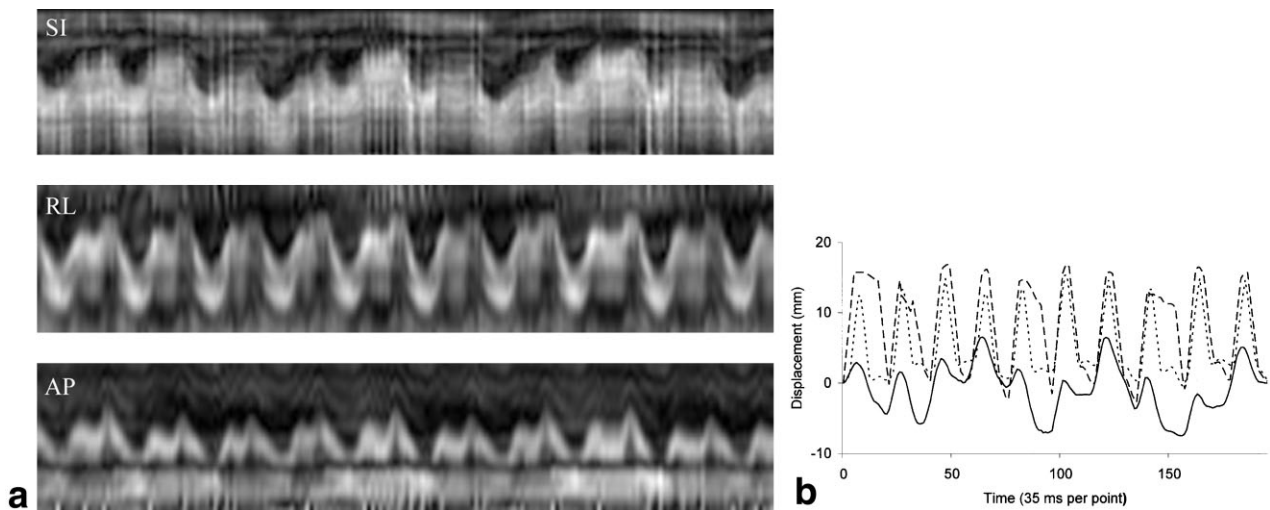
FIG. 5. **a:** The cardiac fat navigator records in image space acquired during free breathing. The SI, RL, and AP portions (FOV = 50 mm) correspond to the three peaks of *k*-space sampling in Fig. 2b. **b:** Corresponding SI (solid), RL (dashed), and AP (dotted) displacements extracted using an image-space least-squares algorithm. The three cycles depicted in SI displacement record were caused by respiration, which affected the other two displacements much less. Accordingly, the SI displacement of the cardiac fat NAV was used for navigator gating.

Motion Correlation Experiment

The diaphragmatic NAV and the cardiac fat NAV were successively acquired during the rest period of the cardiac cycle from four subjects to determine the correlation between the motion of the diaphragm and the heart. The following navigator parameters were used: pencil-beam: length = 180 mm, flip angle = 15°, TR = 15 ms, rbw = ±15.63 kHz; cardiac fat: slab thickness = 50−80 mm, slab FOV = 180 mm, 1-4-6-4-1 type I spatial-spectral RF pulse, flip angle = 30°, TR = 30−35 ms, rbw = ±15.63 kHz. The pencil-beam NAV was placed through the right hemidiaphragm, and the cardiac fat NAV was positioned on the heart volume. The regression coefficient and the correlation coefficient between the two sets of measurements were calculated using linear regression analysis.

Free-Breathing 3D Coronary MRA Experiment

Both the diaphragmatic and cardiac fat NAVs were incorporated into a free-breathing 3D coronary MRA pulse sequence (ECG-triggered segmented *k*-space fast gradient echo) in order to visualize the coronary arteries. This sequence consisted of a predetermined delay after the cardiac trigger, followed by the playout of navigator and fat saturation, and concluded by data readout during the rest period (Fig. 4). Real-time navigator gating was performed on six subjects, using the diaphragmatic navigator or the cardiac fat navigator. The real-time gating program was executed on a workstation (Ultra 1; Sun Microsystems, Palo Alto, CA) that collected navigator data, extracted motion, and controlled data acquisition using the PAWS algorithm (37). Real-time access to the scanner's raw data and instruction memory from the workstation was made possible through a high-speed adapter (SBS Bit 3 Operations, St. Paul, MN). Bin sizes of 1.0 mm and 0.5 mm were used for diaphragmatic and cardiac fat NAVs, respectively, to take into account the linear conversion factor between the respiratory SI movement of the diaphragm and that of the heart (corresponding to a 0.5 conversion factor (6)). The imaging parameters were as follows: TR = 12.5 ms, TE = 1.8 ms, flip angle = 20°, rbw = ±15.63 kHz, 10 slices, slice thickness = 2 mm, in-plane resolution = 1.2 × 1.9 mm², and centric view ordering along k_z. Image quality was rated by three independent viewers on a scale of 1–3: 1 = poor (excessive motion artifacts), 2 = good (mild motion artifacts), and 3 = excellent (negligible motion artifacts).

RESULTS

An example of the image-space cardiac fat navigator records acquired during free breathing is shown in Fig. 5a. Here the horizontal axis represents time, and the vertical axis represents position. Each vertical line displays in grayscales the image-space profile of the collapsed fat signal along a specific direction, and was obtained by taking a 1D Fourier transform of the corresponding peak in the *k*-space navigator data. Figure 5b illustrates the 3D displacements extracted from the records in Fig. 5a, and demonstrates that respiratory motion affects the coronary arteries predominantly in the SI direction.

Figure 6a shows an example of the SI positions of the diaphragm (open triangle) and the coronary arteries (solid circle) obtained over 60 heartbeats using diaphragmatic and cardiac fat NAVs, respectively. The data points are connected to improve the visual similarity between them. Figure 6b presents the same data set on a scatterplot, along with the linear regression line. For this case, the regression coefficient (the slope of the regression line) was 0.44, and the correlation coefficient was 0.95. Over the four subjects, the average regression coefficient was 0.47, and the average correlation coefficient was 0.94. The large correlation coefficient demonstrated the high sensitivity of the cardiac fat navigator in monitoring respiratory motion.
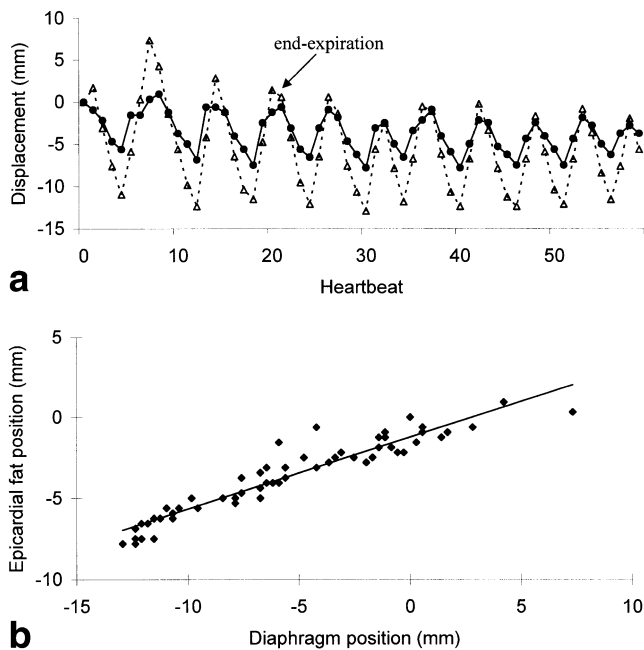
FIG. 6. **a:** SI positions of diaphragm (△) and epicardial fat (●) detected by diaphragmatic and cardiac fat NAVs, respectively, in mid-diastole over 60 heartbeats. **b:** The same set of data presented on a scatterplot along with the linear regression line: [epicardial fat position] = 0.44*[diaphragm position] − 1.23 mm, r = 0.95.

Figure 7 illustrates a case in which both cardiac fat navigator gating and diaphragmatic navigator gating substantially reduced ghosting and blurring artifacts, and provided similar image quality. Figure 8 demonstrates a case in which the cardiac fat NAV provided better image quality than the diaphragmatic NAV. Overall, compared to the diaphragmatic navigator gating, the cardiac fat navigator gating showed similar quality in three subjects and better quality in three subjects. In addition to better image quality, the cardiac fat navigator gating also provided a slightly shorter scan time than the diaphragmatic navigator gating (50% vs. 46% in terms of average scan efficiencies). The results are summarized in Table 1.

DISCUSSION

Our preliminary data demonstrate that the cardiac fat NAV can track bulk translation of the epicardial fat at a 30–35-ms frame rate, and provides better quality and shorter scan times for coronary MRA compared to diaphragmatic navigator gating. These results tend to confirm our hypothesis that the quality of navigator coronary MRA can be improved by improving the accuracy of detecting coronary motion. The cardiac fat navigator approach offers a means of rapidly and accurately measuring this motion.

Adaptive motion-correction algorithms used in navigator coronary MRA, such as the slice-following algorithm (10), may benefit even more from the cardiac fat NAV than the gating algorithms evaluated in this study. The subject-specific conversion factor that relates the position of the diaphragm to that of the coronary arteries is eliminated. Furthermore, any residual chest wall ghosting artifacts are reduced by the spatial saturation employed in the cardiac fat NAV.

The fundamental premise of the cardiac fat NAV is that >90% of the cardiac motion of coronary bifurcations consists of global motion, i.e., linear translation, rotation, and dilation/contraction (29). Although our study did not correlate motion of the epicardial fat with that of the proximal coronary arteries, the spatial connectivity between these tissues implies that they undergo the same global motion. Therefore, the cardiac fat NAV offers a direct measure of global coronary motion, which is a major component of coronary motion. Furthermore, all components of the global coronary motion can be encoded in a single *k*-space sampling trajectory and extracted simultaneously, permitting rapid and accurate motion measurement. This global motion information can be used to compensate for global motion artifacts in coronary MRA through motion-correction mechanisms (e.g., phase shift for translation, gradient rotation for rotation, and a combination of phase shift and scaling for dilation). The local deformation of coronary arteries, which is difficult to estimate by navigator, is proportional to global motion; hence, the imaging artifacts of local motion can be reduced by limiting the global motion range using navigator gating algorithms. Therefore, the cardiac fat NAV may be an effective approach to min-
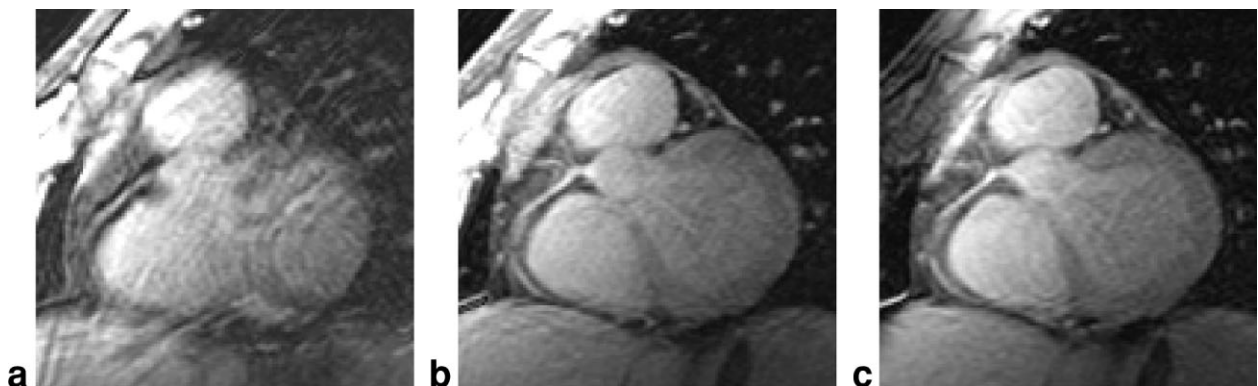

FIG. 7. Coronary MRA images of subject A obtained (**a**) without navigator gating, (**b**) with diaphragmatic gating, and (**c**) with cardiac fat gating. Cardiac fat navigator gating and diaphragmatic navigator gating provided similar image quality.
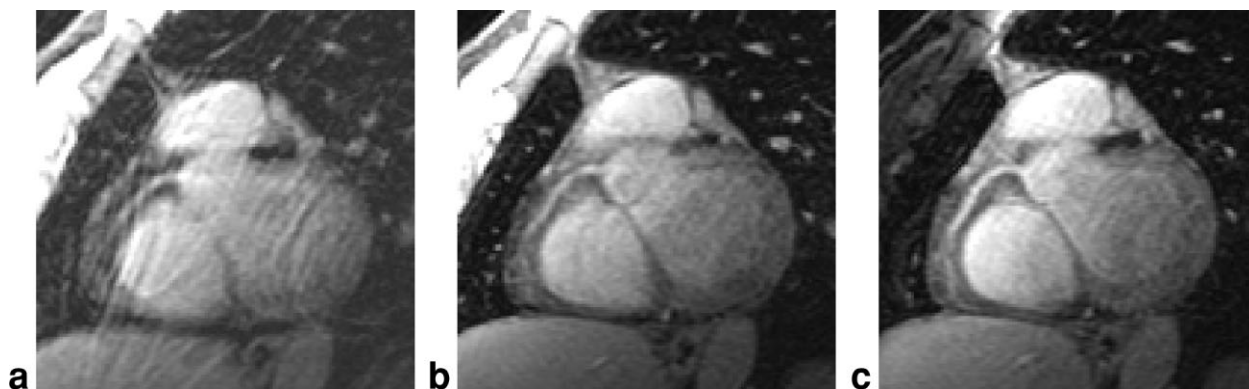
FIG. 8. Coronary MRA images of subject C obtained (**a**) without navigator gating, (**b**) with diaphragmatic gating, and (**c**) with cardiac fat gating. Cardiac fat navigator gating provided better image quality compared to diaphragmatic navigator gating.

imize both global and local motion artifacts in coronary MRA.

In this preliminary study we evaluated the usefulness of the cardiac fat NAV in detecting respiratory motion of coronary arteries. The SI displacements of the cardiac fat NAV were found to be linearly correlated to the SI displacements of the diaphragm NAV with an average regression coefficient of 0.47, which is slightly lower than the previously reported value (6). This discrepancy was likely caused by the difference in the location of the diaphragmatic NAV in these two studies. In the present study the diaphragmatic NAV was positioned on the right hemidiaphragm, which translates in a greater range than the left diaphragm point immediately below the heart (as used in the previous study).

The cardiac fat NAV can be readily applied to monitor cardiac motion and compensate for its effects in general cardiac MRI. Currently the electrocardiogram (ECG) is used to gate cardiac MR data acquisitions; however, the ECG signal does not provide any direct measure of cardiac contraction. Substantial cardiac motion can occur under ECG guidance. The use of the cardiac fat NAV immediately before and after data acquisition would eliminate this problem.

This preliminary implementation of the cardiac fat NAV contains several limitations that may have contributed to the observed "slight" improvement over diaphragmatic NAV in coronary MRA. Only the SI displacement of the cardiac fat NAV was utilized for navigator gating. Accounting for residual translations in RL and AP directions, and using more sophisticated k-space trajectories to detect bulk rotation and dilation (25) can lead to more effective motion suppression. The epicardial fat navigator signal can be contaminated by the chest wall signal, particularly when a surface coil is used for signal reception. The degree of contamination must be evaluated quantitatively. A more effective spatial saturation pulse of shorter duration is desired, and other means of implementing the spatial-spectral selective excitation must be explored. A surface coil array that shifts the coil sensitivity toward the heart (38) should be employed for signal reception.

In conclusion, the cardiac fat NAV provides a fast, direct, and sensitive means of measuring bulk coronary motion, and can be utilized to monitor, and compensate for, motion effects in navigator cardiac MRI.

Table 1
Quality Scores and Scan Efficiencies of Coronary MRA Obtained With Diaphragmatic and Cardiac Fat Navigator Gating, Respectively

Subject	Diaphragmatic gating		Cardiac fat gating	
	Image quality	Scan efficiency (%)	Image quality	Scan efficiency (%)
A	3	60	3	50
B	2.3	54	3	48
C	2.3	49	3	42
D	2	38	2.7	57
E	2	43	2	46
F	3	41	3	62
Average	2.4	46	2.8	50

Rating was done by three independent viewers using the following scale: 1, poor (excessive artifacts); 2, good (mild artifacts); 3, excellent (negligible artifacts).

REFERENCES

1. Edelman RR, Manning WJ, Burstein D, Paulin S. Coronary arteries: breath-hold MR angiography. Radiology 1991;181:641–643.
2. Manning WJ, Li W, Boyle NG, Edelman RR. Fat-suppressed breath-hold magnetic resonance coronary angiography. Circulation 1993;87:94–104.
3. Ehman RL, Felmlee JP. Adaptive techniques for high definition MR imaging of moving structures. Radiology 1988;173:255–263.
4. Holland AE, Goldfarb JW, Edelman RR. Diaphragmatic and cardiac motion during suspended breathing: preliminary experience and implications for breath-hold MR imaging. Radiology 1998;209:483–489.
5. Pauly J, Nishimura D, Macovski A. A k-space analysis of small-tip-angle excitation. J Magn Reson 1989;81:43–56.
6. Wang Y, Riederer SJ, Ehman RL. Respiratory motion of the hearts: kinematics and the implications for the spatial resolution of coronary MR imaging. Magn Reson Med 1995;33:713–719.

7. Oshinski JN, Hofland L, Mukundan Jr S, Dixon WT, Parks WJ, Pettigrew RI. Two-dimensional coronary MR angiography without breath holding. Radiology 1996;201:737–743.
8. Wang Y, Rossman PJ, Grimm RC, Riederer SJ, Ehman RL. Navigator-based real-time respiratory gating and triggering for reduction of respiration effects in three-dimensional coronary MR imaging. Radiology 1996;198:55–60.
9. Li D, Kaushikkar S, Haacke EM, Woodard PK, Dhawale PJ, Kroeker RM, Laub G, Kuginuki Y, Gutierrez FR. Coronary arteries: three-dimensional MR imaging with retrospective respiratory gating. Radiology 1996;201:857–863.
10. Danias PG, McConnell MV, Khasgiwala VC, Chuang ML, Edelman RR, Manning WJ. Prospective navigator correction of slice position for coronary magnetic resonance angiography. Radiology 1997;203:733–736.
11. Stuber M, Botnar RM, Danias PG, Sodickson DK, Kissinger KV, Van Cauteren M, De Becker J, Manning WJ. Double-oblique free-breathing high resolution three-dimensional coronary magnetic resonance angiography. J Am Coll Cardiol 1999;34:524–531.
12. Wang Y, Ehman RL. Retrospective adaptive motion correction for navigator-gated 3D coronary MR angiography. J Magn Reson Imaging 2000;11:208–214.
13. Lethimonnier F, Furber A, Morel O, Geslin P, L'Hoste P, Tadei A, Jallet P, Caron-Poitreau C, Le Jeune JJ. Three-dimensional coronary artery MR imaging using prospective real-time respiratory navigator and linear phase shift processing: comparison with conventional coronary angiography. Magn Reson Imaging 1999;17:1111–1120.
14. Sardanelli F, Molinari G, Zandrino F, Balbi M. Three-dimensional, navigator-echo MR coronary angiography in detecting stenoses of the major epicardial vessels, with conventional coronary angiography as the standard of reference. Radiology 2000;214:808–814.
15. Kim WY, Danias PG, Stuber M, Flamm SD, Plein S, Nagel E, Langerak SE, Weber OM, Pedersen EM, Schmidt M, Botnar RM, Manning WJ. Coronary magnetic resonance angiography for the detection of coronary stenoses. N Engl J Med 2001;345:1863–1869.
16. Watanabe Y, Nagayama M, Amoh Y, Fujii M, Fuku Y, Okumura A, Van Cauteren M, Stuber M, Dodo Y. High-resolution selective three-dimensional magnetic resonance coronary angiography with navigator-echo technique: segment-by-segment evaluation of coronary artery stenosis. J Magn Reson Imaging 2002;16:238–245.
17. Wittlinger T, Voigtlander T, Rohr M, Meyer J, Thelen M, Kreitner KF, Kalden P. Magnetic resonance imaging of coronary artery occlusions in the navigator technique. Int J Cardiovasc Imaging 2002;18:203–211.
18. Nikolaou K, Huber A, Knez A, Becker C, Bruening R, Reiser M. Intra-individual comparison of contrast-enhanced electron-beam computed tomography and navigator-echo-based magnetic resonance imaging for noninvasive coronary artery angiography. Eur Radiol 2002;12:1663–1671.
19. Ropers D, Regenfus M, Stilianakis N, Birke S, Kessler W, Moshage W, Laub G, Daniel WG, Achenbach S. A direct comparison of noninvasive coronary angiography by electron beam tomography and navigator-echo-based magnetic resonance imaging for the detection of restenosis following coronary angioplasty. Invest Radiol 2002;37:386–392.
20. Bunce NH, Jhooti P, Keegan J, Rahman SL, Bunce C, Firmin DN, Davies SW, Lorenz CH, Pennell DJ. Evaluation of free-breathing three-dimensional magnetic resonance coronary angiography with hybrid ordered phase encoding (HOPE) for the detection of proximal coronary artery stenosis. J Magn Reson Imaging 2001;14:677–684.
21. Nehrke K, Bornert P. Study of the respiratory motion of the heart using multiple navigator pulses. In: Proceedings of the 8th Annual Meeting of ISMRM, Denver, 2000. p 404.
22. Sachs TS, Meyer CH, Pauly JM, Hu BS, Nishimura DG, Macovski A. The real-time interactive 3D-DVA for robust coronary MRA. IEEE Trans Med Imaging 2000;19:73–79.
23. Stuber M, Botnar RM, Danias PG, Kissinger KV, Manning WJ. Submillimeter three-dimensional coronary MR angiography with real-time navigator correction: comparison of navigator locations. Radiology 1999;212:579–587.
24. Fu ZW, Wang Y, Grimm RC, Rossman PJ, Felmlee JP, Riederer SJ, Ehman RL. Orbital navigator echoes for motion measurements in magnetic resonance imaging. Magn Reson Med 1995;34:746–753.
25. Welch EB, Manduca A, Grimm RC, Ward HA, Jack Jr CR. Spherical navigator echoes for full 3D rigid body motion measurement in MRI. Magn Reson Med 2002;47:32–41.
26. Wang Y, Grimm RC, Felmlee JP, Riederer SJ, Ehman RL. Algorithms for extracting motion information from navigator echoes. Magn Reson Med 1996;36:117–123.
27. Foo TK, King KF. A computationally efficient method for tracking reference position displacements for motion compensation in magnetic resonance imaging. Magn Reson Med 1999;42:548–553.
28. Nguyen TD, Wang Y, Watts R, Mitchell I. *k*-Space weighted least-squares algorithm for accurate and fast motion extraction from magnetic resonance navigator echoes. Magn Reson Med 2001;46:1037–1040.
29. Potel MJ, MacKay SA, Rubin JM, Aisen AM, Sayre RE. Three-dimensional left ventricular wall motion in man. Coordinate systems for representing wall movement direction. Invest Radiol 1984;19:499–509.
30. Meyer CH, Pauly JM, Macovski A, Nishimura DG. Simultaneous spatial and spectral selective excitation. Magn Reson Med 1990;15:287–304.
31. Schick F, Forster J, Machann J, Huppert P, Claussen CD. Highly selective water and fat imaging applying multislice sequences without sensitivity to B1 field inhomogeneities. Magn Reson Med 1997;38:269–274.
32. Zur Y. Design of improved spectral-spatial pulses for routine clinical use. Magn Reson Med 2000;43:410–420.
33. Bracewell RN. The Fourier transform and its applications. San Francisco: McGraw-Hill Book Company; 1978.
34. Souza SP, Szumowski J, Dumoulin CL, Plewes DP, Glover G. SIMA: simultaneous multislice acquisition of MR images by Hadamard-encoded excitation. J Comput Assist Tomogr 1988;12:1026–1030.
35. Pauly J, Le Roux P, Nishimura D, Macovski A. Parameter relations for the Shinnar-Le Roux selective excitation pulse design algorithm. IEEE Trans Med Imaging 1991;10:53–65.
36. Wang Y, Christy PS, Korosec FR, Alley MT, Grist TM, Polzin JA, Mistretta CA. Coronary MRI with a respiratory feedback monitor: the 2D imaging case. Magn Reson Med 1995;33:116–121.
37. Jhooti P, Keegan J, Gatehouse PD, Collins S, Rowe A, Taylor AM, Firmin DN. Phase reordering with automatic window selection (PAWS): a novel motion-resistant technique for 3D coronary imaging. Magn Reson Med 2000;43:470–480.
38. Bottomley PA, Lugo Olivieri CH, Giaquinto R. What is the optimum phased array coil design for cardiac and torso magnetic resonance? Magn Reson Med 1997;37:591–599.